

A Ground-Motion Model for GNSS Peak Ground Displacement

Dara E. Goldberg¹ , Diego Melgar² , Gavin P. Hayes¹ , Brendan W. Crowell³ , and Valerie J. Sahakian² 

ABSTRACT

We present an updated ground-motion model (GMM) for M_w 6–9 earthquakes using Global Navigation Satellite Systems (GNSS) observations of the peak ground displacement (PGD). Earthquake GMMs inform a range of Earth science and engineering applications, including source characterization, seismic hazard evaluations, loss estimates, and seismic design standards. A typical GMM is characterized by simplified metrics describing the earthquake source (magnitude), observation distance, and site terms. Most often, GMMs are derived from broadband seismometer and accelerometer observations, yet during strong shaking, these traditional seismic instruments are affected by baseline offsets, leading to inaccurate recordings of low-frequency ground motions such as displacement. The incorporation of geodetic data sources, particularly for characterizing the unsaturated ground displacement of large-magnitude events, has proven valuable as a complement to traditional seismic approaches and led to the development of an initial point-source GMM based on PGD estimated from high-rate GNSS data. Here, we improve the existing GMM to more effectively account for fault finiteness, slip heterogeneity, and observation distance. We evaluate the limitations of the currently available GNSS earthquake data set to calibrate the GMM. In particular, the observed earthquake data set is lacking in observations within 100 km of large-magnitude events ($M_w > 8$), inhibiting evaluation of fault dimensions for earthquakes too large to be represented as point sources in the near field. To that end, we separately consider previously validated synthetic GNSS waveforms within 10–1000 km of M_w 7.8–9.3 Cascadia subduction zone scenario ruptures. The synthetic data highlight the importance of fault distance rather than point-source metrics and improve our preparedness for large-magnitude earthquakes with spatiotemporal qualities unlike those in our existing data set.

KEY POINTS

- We develop a regional ground-motion model for peak ground displacement using GNSS observations.
- Scenario ruptures clarify the advantage of generalized mean rupture distance to model near-field displacements.
- Generalized mean rupture distance reduces need for more complexity in the ground-motion model functional form.

INTRODUCTION

In the seconds to minutes following a significant earthquake, earthquake source properties (e.g., hypocentral location, magnitude, style of faulting) provide a basic estimate of the affected area and are then used as input to ground-motion models (GMMs) to estimate, in conjunction with measured ground-motion observations, the intensity of shaking in the surrounding regions. Incorporating GMMs into rapid earthquake response (e.g., the U.S. Geological Survey product

ShakeMap; Wald *et al.*, 2005) is crucial for estimating the expected damage on a local and regional scale and can be used to prioritize and mobilize emergency resources and personnel. GMMs are constructed to relate a chosen ground-motion intensity measure to the earthquake magnitude (source), the observation distance (path), and local-scale geology (site). The most common intensity measures are peak ground acceleration (PGA) and peak ground velocity (PGV), both observed in the time domain, and spectral acceleration (SA), the peak responses of single-degree-of-freedom harmonic oscillators

1. U.S. Geological Survey, Geologic Hazards Science Center, Golden, Colorado, U.S.A.,  <https://orcid.org/0000-0002-0923-3180> (DEG);  <https://orcid.org/0000-0003-3323-0112> (GPH); 2. Department of Earth Sciences, University of Oregon, Eugene, Oregon, U.S.A.,  <https://orcid.org/0000-0001-6259-1852> (DM);  <https://orcid.org/0000-0002-3278-4458> (VIS); 3. Department of Earth and Space Sciences, University of Washington, Seattle, Washington, U.S.A.,  <https://orcid.org/0000-0001-7096-601X> (BWC)

*Corresponding author: degoldberg@usgs.gov

Cite this article as Goldberg, D. E., D. Melgar, G. P. Hayes, B. W. Crowell, and V. J. Sahakian (2021). A Ground-Motion Model for GNSS Peak Ground Displacement, *Bull. Seismol. Soc. Am.* **111**, 2393–2407, doi: [10.1785/0120210042](https://doi.org/10.1785/0120210042)

© Seismological Society of America

(typically damped to 5% of critical) observed in the frequency domain. Here, we extend the time-domain approaches to the design of a GMM for the intensity measure peak ground displacement (PGD). The inclusion of PGD essentially completes the broadband sampling of time-domain intensity measures; PGA is observed at high frequencies, PGD at low frequencies, with PGV observed at frequencies in between.

GNSS PGD

Until recent proliferation of high-rate (HR) Global Navigation Satellite Systems (GNSS) instrumentation, PGD was underutilized in GMM studies because seismic ground displacement at near-field and regional distances is challenging to measure using traditional inertial instrumentation such as broadband seismometers and accelerometers (e.g., Campbell and Bozorgnia, 2008). Near-field studies of moderate- to large-magnitude events have generally relied on strong-motion (SM) accelerometers, which are designed with low gains to avoid clipping during intense ground shaking. Unmodeled tilts and rotations present in inertial observations prevent the reliable recording of the three separate components of translational motion and contribute to baseline offsets that inhibit proper integration, leading to unphysical linear drifts in estimated velocities (single integration) and quadratic drifts in estimated displacements (double integration) (e.g., Boore and Bommer, 2005). The process therefore requires either function fitting or implementation of a high-pass filter to remove unphysical drifts, simultaneously resulting in removal of the true long-period portion of the spectrum, most notably, the permanent (or static) offset.

Dynamic displacements are similarly affected, though the extent of reduction is not always obvious because the waveform may appear visually realistic once drift has been removed (e.g., Fig. 1). Comparison between collocated seismic and geodetic sites in Japan during the M_w 9.1 Tohoku-Oki earthquake found that frequency content at periods longer than ~ 10 s was not well recorded by accelerometers (Melgar *et al.*, 2013). So, although peak displacements are sometimes reported as inferred from inertial seismic instrumentation (e.g., Trugman *et al.*, 2019), we stress that PGD measured using filtered inertial instrumentation is inaccurate at regional distances for moderate and larger earthquakes. In comparison, GNSS involve noninertial instruments that measure displacement directly with respect to an absolute reference frame. They are, therefore, unaffected by the baseline offsets that plague inertial instruments and can be considered “ground truth” for earthquake displacements.

To clarify the inaccuracies of using accelerometer observations to measure ground displacement, consider the SM accelerometer station MYG011 (Fig. 1a) and the collocated GNSS station 0550 (Fig. 1b) as they observed the 2011 M_w 9.1 Tohoku-Oki earthquake from a hypocentral distance of ~ 82 km. We focus on the east-component recordings, the

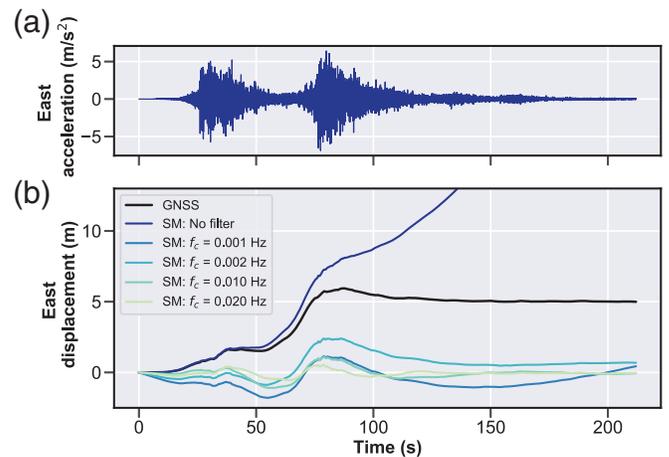


Figure 1. Comparison between Global Navigation Satellite Systems (GNSS) station 0550 and collocated strong-motion (SM) accelerometer station MYG011 time series during the 2011 M_w 9.1 Tohoku-Oki earthquake. (a) SM station MYG011 acceleration time series. (b) GNSS station 0550 displacements (black) compared with displacements from twice-integrated SM records at MYG011. The darkest blue line shows the twice-integrated SM accelerometer record, with no filtering applied. Remaining waveforms show the accelerometer-derived displacements subject to high-pass filters with various corner frequencies. The accelerometer-derived waveform high-pass filtered to 0.001 Hz (1000 s) records the most similar maximum displacement to the GNSS ground truth but does not remove enough long-period signal to avoid unphysical drift later in the waveform and will presumably exceed the true maximum displacement beyond the 200 s shown.

primary component of motion during that event. For comparison, the accelerations recorded by the SM accelerometer have been integrated twice to displacements (Fig. 1b). The unfiltered accelerometer record (darkest blue) demonstrates the quadratic growth expected for double integration without removal of baseline offsets. The remaining colored lines show this same signal high-pass filtered, as is typical practice for removing unphysical drift, to different filter corner frequencies. None of the filters can resolve the eastward static (permanent) offset that is recorded easily with GNSS (black). Furthermore, although the time series filtered to $f_c = 0.001$ Hz (1000 s) provides the best estimate of maximum displacement (consistent with recent work by Zhang *et al.*, 2020), the waveform becomes unrealistic following this peak value, returning to quadratic drift. More severe filter corner frequencies further restrict the maximum displacement. This comparison between SM accelerometer-derived displacements and displacements observed directly at collocated GNSS receivers is an example of the inertial instrument’s loss of fidelity at long periods. As a result, GNSS is now recognized as a valuable complement to traditional seismic observations, particularly to resolve these low-frequency seismic signals.

Ultimately, broadband ground displacement is challenging to record with traditional inertial seismic observation tools

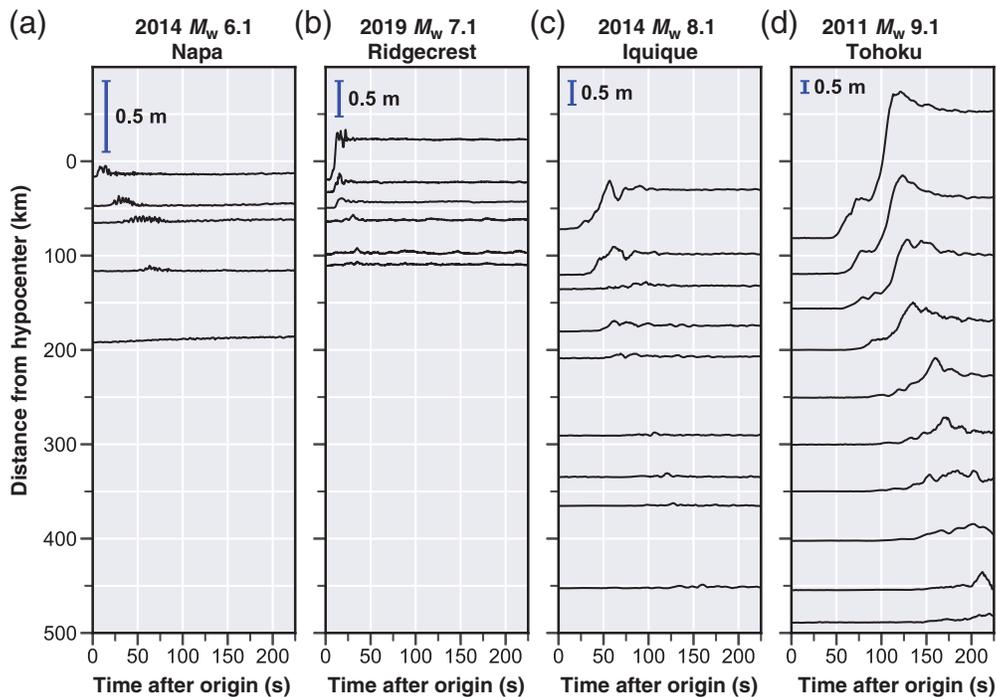


Figure 2. Example GNSS waveforms at a range of hypocentral distances, observed during moderate- to large-magnitude earthquakes in a variety of tectonic settings: (a) 2014 M_w 6.1 Napa, California, (b) 2019 M_w 7.1 Ridgecrest, California, (c) 2014 M_w 8.1 Iquique, Chile, and (d) 2011 M_w 9.1 Tohoku-Oki, Japan. Waveforms are offset by their distance from the earthquake hypocenter. Note the different vertical scaling of waveform amplitudes in each subfigure, given by the blue scale bar in the top left corner of each panel.

alone and instead requires independent information from non-inertial geodetic data sets such as HR GNSS. These properly recorded displacement waveforms show clear patterns that demonstrate their utility for rapid earthquake response. First, it is well established that the permanent (0 Hz) displacement as a result of an earthquake is diagnostic of the earthquake magnitude (Crowell *et al.*, 2012). Indeed, moment magnitude by definition is proportional to the product of the shear modulus, the fault dimensions, and the average permanent displacement across the fault. Thus, accounting for distance and azimuth to the fault can relate the permanent displacement at a receiver station to the magnitude of the observed earthquake (e.g., Petersen *et al.*, 2011). PGD, though related, is a distinct metric from the permanent displacement. PGD is the maximum value of the square root of the three-component sum of squares of an HR (≥ 1 Hz) displacement time series. It is an arguably more useful metric than permanent displacement in practice, because dynamic displacements generally exceed static displacements, meaning that stations observing either small events or located farther from the event may observe dynamic displacements even if no permanent deformation occurs. This is especially valuable because GNSS has a higher noise floor than familiar inertial instrumentation: ~ 5 cm for periods shorter than 100 s and ~ 1 cm for periods shorter than 10 s in real-time GNSS (Melgar *et al.*,

2020). To highlight the relation between static and dynamic displacements at varying observation distances, consider example waveforms from four earthquakes each differing by one magnitude unit: the 2014 M_w 6.1 Napa, California, the 2019 M_w 7.1 Ridgecrest, California, the 2014 M_w 8.1 Iquique, Chile, and the 2011 M_w 9.1 Tohoku-Oki, Japan, earthquakes (Fig. 2; note the different vertical scaling on each subfigure). For the smallest event (2014 M_w 6.1 Napa, California), even the closest stations show negligible static displacement, though dynamic displacements are visible above the noise beyond 100 km from the hypocenter. The utility of GNSS quickly diminishes for earthquakes $M_w < 6$, because even dynamic displacements at near-field stations may not exceed the GNSS noise floor. For the larger events, the

PGD temporarily exceeds the final permanent displacement, by as much as $\sim 15\%$ – 20% , as the large amplitude S and surface waves pass the GNSS station location.

Reviewing GMMs

The observation that PGD increases for larger magnitude earthquakes and decreases with distance from the source led to the development of a simple scaling relation between GNSS-derived PGD, earthquake magnitude, M_w , and hypocentral distance, R_{hyp} (Crowell *et al.*, 2013):

$$\log_{10} \text{PGD} = A + B \times M_w + C \times M_w \times \log_{10} R_{hyp}. \quad (1)$$

Equation (1), hereafter referred to as C13 (for Crowell *et al.*, 2013), illustrates that PGD attenuates log-linearly with hypocentral distance, R_{hyp} , in which A , B , and C are constants estimated from available GNSS-observed earthquakes. This scaling relation, originally used for rapid magnitude estimation from PGD, has been updated as new data become available (Melgar, Crowell, *et al.*, 2015; Ruhl *et al.*, 2018), applied to studies of rupture initiation characteristics (Goldberg *et al.*, 2018), and used to accurately estimate the magnitudes of recent significant earthquakes (e.g., Grapenthin *et al.*, 2017; Hodgkinson *et al.*, 2020). C13 includes an overall bias term, a magnitude scaling term, and a magnitude-dependent geometrical spreading term.

We will also consider a more complex ground-motion functional form proposed by [Thompson and Baltay \(2018\)](#) for application to PGA, PGV, and SA intensity measures. For our purposes, we simplify to include only magnitude and distance terms to relate to our chosen intensity measure, PGD:

$$\log_{10}(\text{PGD}) = c_0 + F_R + F_M, \quad (2)$$

in which F_R and F_M are the distance-scaling term and magnitude-scaling term, respectively, and are given by

$$\begin{aligned} F_R &= (c_{R0} + c_{R1}M_w) \log_{10} R_{\text{hyp}} + c_{R2}R_{\text{hyp}} \\ F_M &= c_{M1}M_w + c_{M2} \ln(1 + e^{-M_w}), \end{aligned} \quad (3)$$

in which c_0 , c_{R0} , c_{R1} , c_{R2} , c_{M1} , and c_{M2} are constants determined empirically. The F_M term itself is simplified to consider only large-magnitude terms, because the GNSS data should not be used to consider small-magnitude events. We will refer to equation (2) as TB18 (for [Thompson and Baltay, 2018](#)).

Although the magnitude dependence in the distance-attenuation terms in both C13 and TB18 accounts somewhat for the expected increase in fault dimensions for larger magnitude earthquakes, the use of the hypocentral distance metric largely maintains the assumption that the earthquakes can be modeled as point sources. Hypocentral distance is a convenient metric for the original intention of C13, rapid magnitude estimation for earthquake and tsunami early warning ([Melgar, Crowell, et al., 2015](#); [Goldberg and Bock, 2017](#); [Williamson et al., 2020](#)). An earthquake's hypocentral location can be pinpointed seconds after initial data acquisition, meaning the distance from earthquake origin to regional stations can be calculated with negligible delay. However, moderate- to large-magnitude earthquakes can be tens or even hundreds of kilometers in length (e.g., [Blaser et al., 2010](#); [Allen and Hayes, 2017](#); [Thingbaijam et al., 2017](#)). In the near field especially, the point-source assumption may be a poor indicator of expected ground motion. The relaxed time requirements of ground-motion prediction, as opposed to early warning, allow us to add more complexity to the equation, solidifying the relationship for future use on earthquakes yet imagined. Specifically, as finite-fault modeling becomes faster and more automated (e.g., [Zheng et al., 2020](#)), it becomes practical to account for effects such as fault finiteness and slip heterogeneity in regional ground-motion predictions, perhaps even on timescales relevant to rapid response.

In this article, we update the observed earthquake GNSS PGD data set used to estimate the C13 GMM coefficients and consider limitations of the available data set to create a robust GMM for PGD. We supplement the observed earthquake data set with synthetic data, identifying earthquake rupture characteristics that are poorly described by the existing equation. We consider the effects of fault finiteness and slip heterogeneity by exploring the generalized mean rupture

distance metric as a substitute for hypocentral distance ([Thompson and Baltay, 2018](#)). Finally, we assess the value of additional complexity in the function form of the ground-motion model by comparing the performance of forms C13 and TB18 and use results from both the observed and scenario data sets to suggest a practical PGD GMM.

DATA AND METHODS

We consider 2371 total HR-GNSS PGD measurements observed during 33 global earthquakes of magnitude 6.0–9.1. Many of these observations were previously reported with example application to early warning magnitude estimation from HR-GNSS PGD using functional form C13 ([Ruhl et al., 2018](#)). We have supplemented that data set with five newly analyzed earthquakes (see Table 1, with newly added earthquakes denoted with a dagger symbol). The new HR-GNSS data not included in [Ruhl et al. \(2018\)](#) were processed with GipsyX Precise Point Positioning software ([Bertiger et al., 2020](#)). The entire data set has been manually inspected to remove any stations without a PGD signal above the station noise. Importantly, this manual inspection removed all the waveforms from event N.Honshu2013, Japan (see [Ruhl et al., 2018](#)); therefore, that event is no longer part of our data set. The total number of observing stations that passed these criteria for each remaining event is listed in Table 1.

First, we simply update the coefficients A , B , and C from C13 with this up-to-date data set using a mixed-effects regression approach, in which coefficients A , B , and C are solved for as fixed effects (e.g., [Barbour and Crowell, 2017](#); [Sahakian et al., 2018](#)). This form includes an event and a site term, E and S , respectively, for all events, i , and stations, j , as random effects that may introduce bias in the model due to data set selection:

$$\log_{10} \text{PGD} = A + B \times M_w + C \times M_w \times \log_{10} R_{\text{hyp}} + E_i + S_j. \quad (4)$$

We additionally report τ , ϕ_S , and ϕ_{SS} , or the standard deviations of all event terms (E_i), site terms (S_j), and remaining residuals or path terms (or site-corrected within-event variability), respectively ([Sahakian et al., 2018](#); [Sahakian, Baltay, et al., 2019](#)). These are representative of the relative biases between the model and random effects, due to data set selection. The overall uncertainty on the model, σ , is also reported, and can be represented as

$$\sigma^2 = \tau^2 + \phi_S^2 + \phi_{SS}^2. \quad (5)$$

The station locations, as well as a count of the number of events each station observed, is available in Figure 3. Because of the global distribution of events, the majority of the stations in the database (754 of 1351) observed only one of the earthquakes. Some stations observed foreshock–mainshock or mainshock–aftershock pairs (see Table 1), and two stations observed eight

TABLE 1

Details of the 33 Observed Events Considered in This Study

Event Name	Country	Origin Time (UTC) (yyyy/mm/dd hh:mm:ss)	Longitude (°E)	Latitude (°N)	Depth (km)	M_w	Number of Stations	Mechanism	Model Source
Tohoku2011	Japan	2011/03/11 T05:46:18	142.3730	38.2970	29.0	9.1	504	Reverse	SRCMOD*
Maule2010	Chile	2010/02/27 T06:34:14	-72.7330	-35.9090	35.0	8.8	19	Reverse	SRCMOD
Illapel2015	Chile	2015/09/16 T22:54:33	-71.6540	-31.5700	29.0	8.3	34	Reverse	SRCMOD
Tokachi2003	Japan	2003/09/25 T19:50:08	144.0785	41.7797	42.0	8.3	238	Reverse	SRCMOD
Tehuantepec2017	Mexico	2017/09/08 T04:49:19	-93.8990	15.0220	47.4	8.2	6	Normal	SRCMOD, Melgar et al. (2018)
Iquique2014	Chile	2014/04/01 T23:46:47	-70.7690	-19.6100	25.0	8.1	22	Reverse	SRCMOD
Ibaraki2011	Japan	2011/03/11 T06:15:35	141.2653	36.1083	43.2	7.9	641	Reverse	SRCMOD, Zheng et al. (2020)
Kodiak2018 [†]	U.S.A.	2018/01/23 T09:31:40	-149.1660	56.0040	14.1	7.9	6	Normal	NEIC [‡]
Ecuador2016	Ecuador	2016/04/16 T23:58:36	-79.9220	0.3820	20.6	7.8	20	Reverse	NEIC
Kaikoura2016	New Zealand	2016/11/13 T11:02:56	173.0540	-42.7370	15.0	7.8	35	Strike slip	NEIC
Nepal2015	Nepal	2015/04/25 T06:11:25	84.7310	28.2310	8.2	7.8	7	Reverse	SRCMOD
Iquique_aftershock2014	Chile	2014/04/03 T02:43:13	-70.4930	-20.5710	22.4	7.7	10	Reverse	NEIC
Mentawai2010	Indonesia	2010/10/25 T14:42:22	100.1140	-3.4840	20.0	7.7	7	Reverse	NEIC
N.Honshu2011	Japan	2011/03/11 T06:25:50	144.8940	37.8367	34.0	7.6	42	Normal	Zheng et al. (2020)
Melinka2016	Chile	2016/12/25 T14:22:26	-74.3910	-43.5170	30.0	7.6	4	Reverse	NEIC
Nicoya2012	Costa Rica	2012/09/05 T14:42:08	-85.3050	10.0860	40.0	7.6	9	Reverse	SRCMOD
GreatSwan2018 [†]	Honduras	2018/01/10 T02:51:33	-83.5200	17.4830	19.0	7.5	6	Strike slip	NEIC
Iwate2011	Japan	2011/03/11 T06:08:53	142.7815	39.8390	31.7	7.4	147	Reverse	SRCMOD, Zheng et al. (2020)
Miyagi2011A	Japan	2011/03/09 T02:45:13	143.2798	38.3285	8.3	7.3	112	Reverse	NEIC
Nepal_aftershock2015	Nepal	2015/05/12 T07:05:19	86.0660	27.8090	15.0	7.3	5	Reverse	NEIC
N.Honshu2012	Japan	2012/12/07 T08:18:21	144.3153	37.8158	46.0	7.2	47	Reverse	Zheng et al. (2020)
ElMayor2010	Mexico	2010/04/04 T22:40:42	-115.2800	32.2590	10.0	7.2	90	Strike slip	SRCMOD
Miyagi2011B	Japan	2011/04/07 T14:32:43	141.9237	38.2028	60.7	7.1	31	Reverse	NEIC
Puebla2017	Mexico	2017/09/19 T18:14:38	-98.4890	18.5500	48.0	7.1	3	Normal	NEIC
Ridgecrest2019 [†]	U.S.A.	2019/07/06 T03:19:53	-117.5990	35.6600	8.0	7.1	23	Strike slip	NEIC, SRCMOD, Goldberg et al. (2020)
Kumamoto2016	Japan	2016/04/15 T16:25:06	130.7630	32.7545	12.5	7.0	228	Strike slip	SRCMOD
Aegean2014	Greece	2014/05/24 T09:25:02	25.3890	40.2890	12.0	6.9	3	Strike slip	Konca et al. (2018)
Mouzaki2018 [†]	Greece	2018/10/25 T22:54:49	20.5570	37.5200	14.0	6.8	7	Reverse	NEIC
E.Fukushima2011	Japan	2011/04/11 T08:16:12	140.6727	36.9457	6.4	6.7	31	Normal	Tanaka et al. (2014)
Lefkada2015	Greece	2015/11/17 T07:10:07	20.6002	38.6650	10.7	6.5	4	Strike slip	Chousianitis et al. (2016)
Ridgecrest_foreshock2019 [†]	U.S.A.	2019/07/04 T17:33:49	-117.5040	35.7050	10.5	6.4	4	Strike slip	SRCMOD, Goldberg et al. (2020)
Napa2014	U.S.A.	2014/08/24 T10:20:44	-122.3100	38.2150	11.0	6.1	19	Strike slip	SRCMOD, Melgar, Geng, et al. (2015)
Parkfield2004	U.S.A.	2004/09/28 T17:15:24	-120.3700	35.8150	7.9	6.0	7	Strike slip	SRCMOD

NEIC, National Earthquake Information Center; SRCMOD, Finite-Source Rupture Model.

*SRCMOD: ([Mai and Thingbaijam, 2014](#)).

[†]Newly added events (not included in the [Ruhl et al., 2018](#) data set).

[‡]NEIC: ([Hayes, 2017](#)).

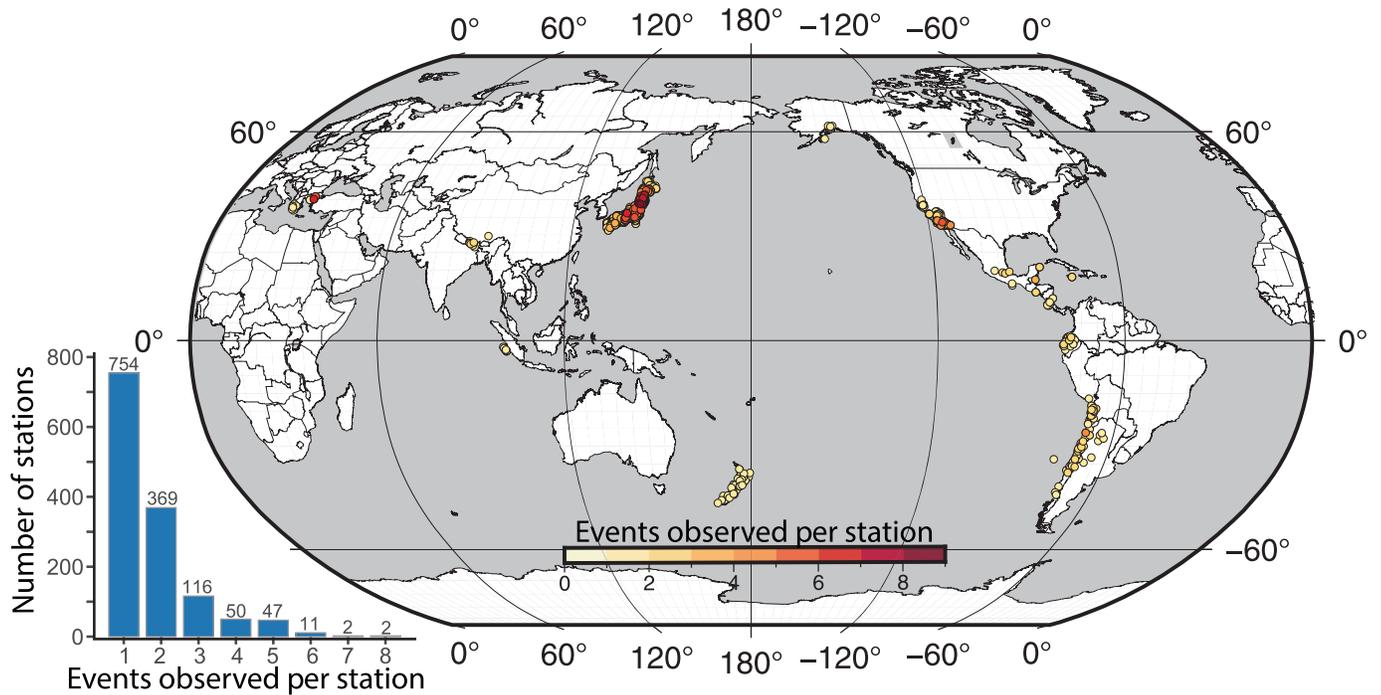


Figure 3. Map showing the locations of high-rate (HR)-GNSS stations in the database, with stations colored by the number of events (Table 1) for which the station recorded a PGD measurement. Most of the stations recorded only one event, and the largest number of events recorded by a single station is eight. The histogram in the bottom left details the total count of stations based on the number of events recorded.

of the events in the Japan region. These statistics will be important for clarifying the interpretation of the event and site terms (see the Discussion section).

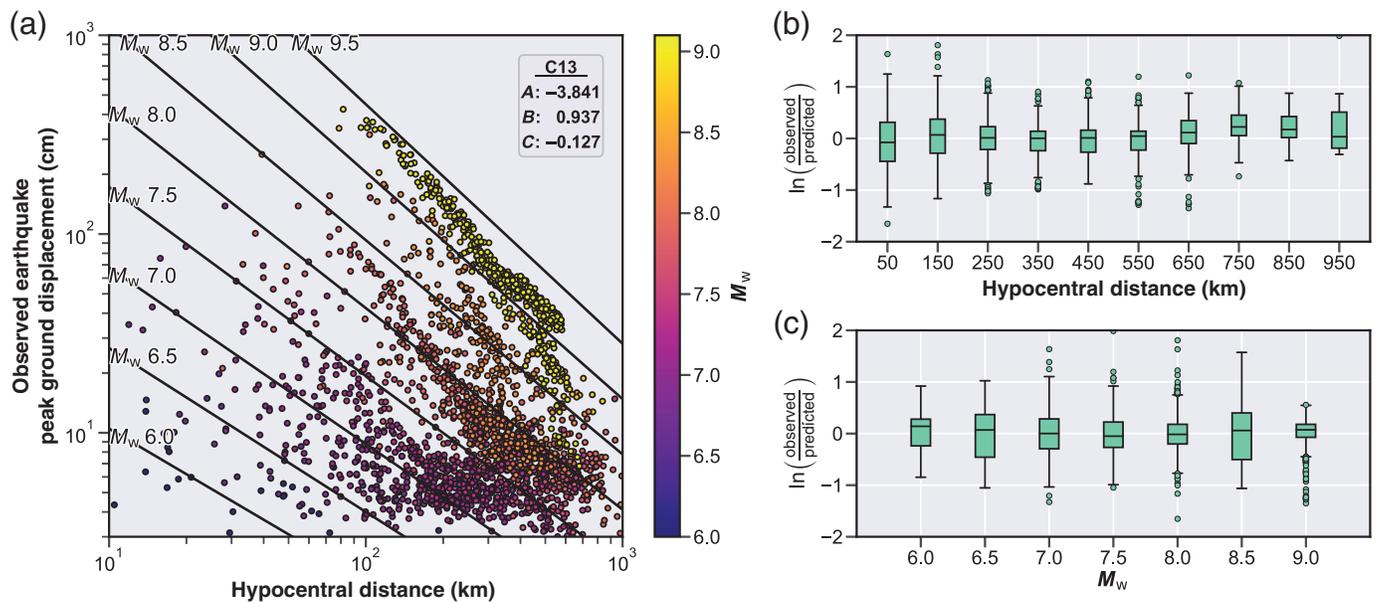
Next, we remove the earthquake point-source assumption implied by C13's reliance on hypocentral distance. It is well known that hypocentral distance is not entirely informative of a location's distance to a seismic event, as the hypocenter is often neither the location of maximum slip, nor the geographic center of slip. Furthermore, the hypocentral distance says nothing of the effects of fault finiteness. Ground-motion studies, therefore, commonly employ more complex distance metrics such as the minimum distance to rupture, R_{RUP} , or the minimum distance to the surface projection of rupture, R_{JB} (in which JB refers to Joyner–Boore), among others. Minimum rupture distances can be problematic, especially at close distances. Instead, we consider the generalized mean rupture distance, a metric that measures the average distance to the fault slip and allows weighting by slip amount and adjustment of the relative weight of the closest and farthest portions of the rupture (Thompson and Baltay, 2018). The generalized mean rupture distance, R_p , of a station is given by

$$R_p = \left(\sum_{i=1}^n w_i R_i^p \right)^{1/p}, \quad (6)$$

in which n is the number of subfaults in the rupture model, R_i is the distance to the i th subfault, w_i is the weight of the i th subfault (normalized to sum to one), and p is the power of the mean. A larger value of p preferentially weights the subfaults at farther distances, whereas a smaller p preferentially weights the closest subfault distances. For an in-depth explanation of values of the power of the mean, p , that can be used in

equation (6) to calculate well-known rupture distances (R_{RUP} , R_{JB} , and so forth), see Thompson and Baltay (2018). The slip models we use to calculate R_p are given in the right column of Table 1 (also see Data and Resources). We use the most up-to-date U.S. Geological Survey finite-fault product when available, in addition to peer-reviewed published models (e.g., Mai and Thingbaijam, 2014). For those earthquakes for which more than one slip model is considered, we calculate the R_p value as the mean value of a station to all available slip models. Low-slip subfaults may be artifacts of the smoothing applied during slip inversions or fitting of noise in the inverted waveforms. We assign the subfault weights, w_i , to be the amount of slip calculated on that subfault in the finite-fault model, which effectively dampens the influence of the inversion noise on the resulting distance calculation.

Based on results to this point, we evaluate the properties of our current data set and supplement our study with 17,413 synthetic HR-GNSS waveforms created for 52 scenario earthquakes of magnitude 7.8–9.3 at the Cascadia subduction zone (FakeQuakes: Melgar et al., 2016; Williamson et al., 2020). These scenario ruptures were generated using a Karhunen–Loève expansion approach to create stochastic slip distributions, and the associated HR (1 Hz) synthetic GNSS waveforms were calculated deterministically, with a 1D velocity model. For



more detail on this synthetic data set, see [Melgar *et al.* \(2016\)](#). The inclusion of these data is intended to identify limitations of our GMM for application to earthquakes beyond the existing GNSS data set. The scenario slip models have no inversion noise, so it should be considered an idealistic case for calculation of the generalized mean rupture distance (equation 6). Finally, in addition to the C13 functional form, we consider the TB18 GMM functional form (equation 2) using the same mixed-effects approach described in equation (4) for application to this scenario earthquake data set.

RESULTS

First, we establish the C13 coefficients from this up-to-date and manually inspected GNSS data set and compare them with previous studies (Table 2). Previous studies using the C13 model calculated the regression coefficients with a linear least-squares approach (“fixed effects”), rather than the mixed-effects regression implemented here ([Crowell *et al.*, 2013](#); [Melgar, Crowell, *et al.*, 2015](#); [Ruhl *et al.*, 2018](#)). This study indicates that the best coefficients for the observed earthquake data set are similar to those determined by [Melgar, Crowell, *et al.* \(2015\)](#), despite the availability of only 10 global earthquakes in that earlier study.

Figure 4. Ground-motion model (GMM) C13 for observed earthquake GNSS data set using hypocentral distance metric: (a) PGD measured at individual GNSS stations versus the hypocentral distance at which that station was located and colored by the magnitude of the earthquake observed. PGD values shown have been adjusted by their corresponding site and event terms. Black lines represent the best-fitting scaling relation (C13) for these data; (b) residual (equation 7) as a function of hypocentral distance; and (c) residual as a function of earthquake magnitude.

The fits of these coefficients to the current data set (Fig. 4a) show no notable bias in either distance (Fig. 4b) or magnitude (Fig. 4c) space. Residuals are calculated as

$$\ln\left(\frac{\text{PGD}^{\text{observed}}}{\text{PGD}^{\text{predicted}}}\right). \quad (7)$$

The model predictions include both fixed and random effects. In Figure 4a (as well as subsequent figures), the plotted PGD values have been adjusted by the corresponding event and site terms. The resulting event terms are available in Table 3 and represent biases from the individual earthquakes. Similarly, site terms (not

TABLE 2

Ground-Motion Model (GMM) Coefficients for the Observed Earthquake Data Set and GMM Form C13 in This Study Compared with Previous Studies

A	B	C	Study
-3.841	0.937	-0.127	This study
-4.434	1.047	-0.138	Melgar, Crowell, <i>et al.</i> (2015)
-6.687	1.500	-0.214	Crowell <i>et al.</i> (2016)*
-5.919	1.009	-0.145	Ruhl <i>et al.</i> (2018)†

*[Crowell *et al.* \(2016\)](#) imposed an exponential distance weighting, favoring closer sites.

†[Ruhl *et al.* \(2018\)](#) considered peak ground displacement (PGD) in meters, whereas the remaining studies, including this one, consider PGD in centimeters.

TABLE 3

Event Terms (E_i) and Standard Error for the 33 Observed Events for GMM Functional Form C13 Using Hypocentral Distance, R_{hyp} , and Generalized Mean Rupture Distance with Exponent -4.5 , $R_p^{-4.5}$

Event	R_{hyp}		$R_p^{-4.5}$	
	Term	Standard Error	Term	Standard Error
Aegean2014	-0.094	0.086	-0.108	0.081
E.Fukushima2011	-0.064	0.031	-0.019	0.030
Ecuador2016	-0.060	0.038	-0.051	0.036
ElMayor2010	0.128	0.018	0.120	0.018
GreatSwan2018	0.151	0.065	0.180	0.062
Ibaraki2011	-0.137	0.007	-0.088	0.007
Illapel2015	-0.294	0.030	-0.253	0.028
Iquique_aftershock2014	-0.176	0.052	-0.155	0.050
Iquique2014	-0.175	0.036	-0.211	0.035
Iwate2011	-0.102	0.014	-0.063	0.014
Kaikoura2016	0.110	0.029	0.065	0.028
Kodiak2018	0.001	0.065	0.039	0.062
Kumamoto2016	0.074	0.012	0.111	0.011
Lefkada2015	0.128	0.077	0.101	0.073
Maule2010	0.169	0.039	0.124	0.037
Melinka2016	-0.033	0.077	0.008	0.073
Mentawai2010	-0.142	0.061	-0.207	0.058
Miyagi2011A	-0.013	0.017	-0.030	0.016
Miyagi2011B	-0.056	0.031	-0.097	0.030
Mouzaki2018	-0.034	0.061	0.033	0.058
N.Honshu2011	-0.012	0.027	0.012	0.025
N.Honshu2012	0.254	0.025	0.249	0.024
Napa2014	0.175	0.039	0.202	0.037
Nepal_aftershock2015	-0.168	0.070	-0.187	0.067
Nepal2015	0.419	0.061	0.208	0.058
Nicoya2012	0.043	0.055	0.077	0.052
Parkfield2004	-0.041	0.061	-0.140	0.058
Puebla2017	-0.122	0.086	-0.072	0.081
Ridgecrest_foreshock2019	-0.014	0.077	-0.008	0.073
Ridgecrest2019	-0.090	0.036	-0.043	0.034
Tehuantepec2017	0.136	0.065	0.110	0.062
Tohoku2011	0.167	0.008	0.211	0.007
Tokachi2003	-0.127	0.011	-0.117	0.011

shown) represent biases from individual stations. These are the equivalent of between-event and site-to-site residuals (Al Atik *et al.*, 2010). Table 4 shows all model uncertainties (equation 5).

Recognizing that the observed earthquake data set is limited—in particular, there is a dearth of observations within 100 km of large-magnitude events ($M_w > 8$)—we are somewhat inhibited in our evaluation of earthquakes too large to be represented as point sources in the near field. To that end, we separately consider previously validated synthetic GNSS waveforms within 10–1000 km of M_w 7.8–9.3 Cascadia subduction zone scenario ruptures (Melgar *et al.*, 2016; Williamson *et al.*, 2020). The same mixed-effects regression approach applied to the scenario ruptures results in a markedly different set of GMM (C13) coefficients (Fig. 5a; Table 4). Although there is again no consistent bias in either distance (Fig. 5b) or magnitude (Fig. 5c) space, the residuals are notably larger than those resulting from the observed earthquake data set.

To test whether the discrepancy between equation coefficients and difference in resulting residuals is due to reliance on the distance metric R_{hyp} —which may be sufficient for the limited observed earthquake data but not for the Cascadia scenario data set that includes synthetic GNSS sites closer to large-magnitude events—we next substitute the generalized mean rupture distance, R_p (equation 6), for hypocentral distance, R_{hyp} , in model C13. We consider a range of powers of the mean, p , from -4.5 to 0 , to encompass the likely best-fitting value for low-frequency intensity measures, as suggested by Thompson and Baltay (2018, see fig. 5 of that study). A comparison between the residuals for each distance definition (Fig. 6) shows that the observed earthquake data set has the lowest residual interquartile range (IQR) for model C13 using the generalized mean rupture distance of power -4.5 , $R_p^{-4.5}$, albeit with similar performance across all values of p and R_{hyp} , indicating that the observed earthquake data set is rather insensitive to distance metric. We use the residual IQR metric, consistent with our representation as boxplots in Figure 6b–d, as a proxy for standard deviation, demonstrating how variable the residuals are. We do not include a figure to show the scaling relation with distance metric $R_p^{-4.5}$, because it is nearly visually indistinguishable from Figure 4 (see the Discussion section). The event terms for model C13 and

TABLE 4

GMM Coefficients and Standard Deviations for Functional Form C13 for Distance Metrics of Interest: R_{hyp} and R_p with Power of the Mean That Minimizes Residual Interquartile Range (IQR)

Data Set	Distance Metric	A	B	C	σ	τ	ϕ_s	ϕ_{SS}
Observed earthquakes	R_{hyp}	-3.841	0.937	-0.127	0.266	0.147	5.9×10^{-5}	0.220
	$R_p^{-4.5}$	-3.841	0.919	-0.122	0.252	0.133	0.000	0.214
Cascadia scenario earthquakes	R_{hyp}	-7.902	1.460	-0.134	0.353	0.169	0.021	0.310
	$R_p^{-2.3}$	-6.527	1.387	-0.171	0.227	0.129	0.032	0.184
Joint	$R_p^{-2.3}$	-5.902	1.303	-0.168	0.255	0.163	0.023	0.195

The final row shows the joint solution for observed and scenario earthquakes together.

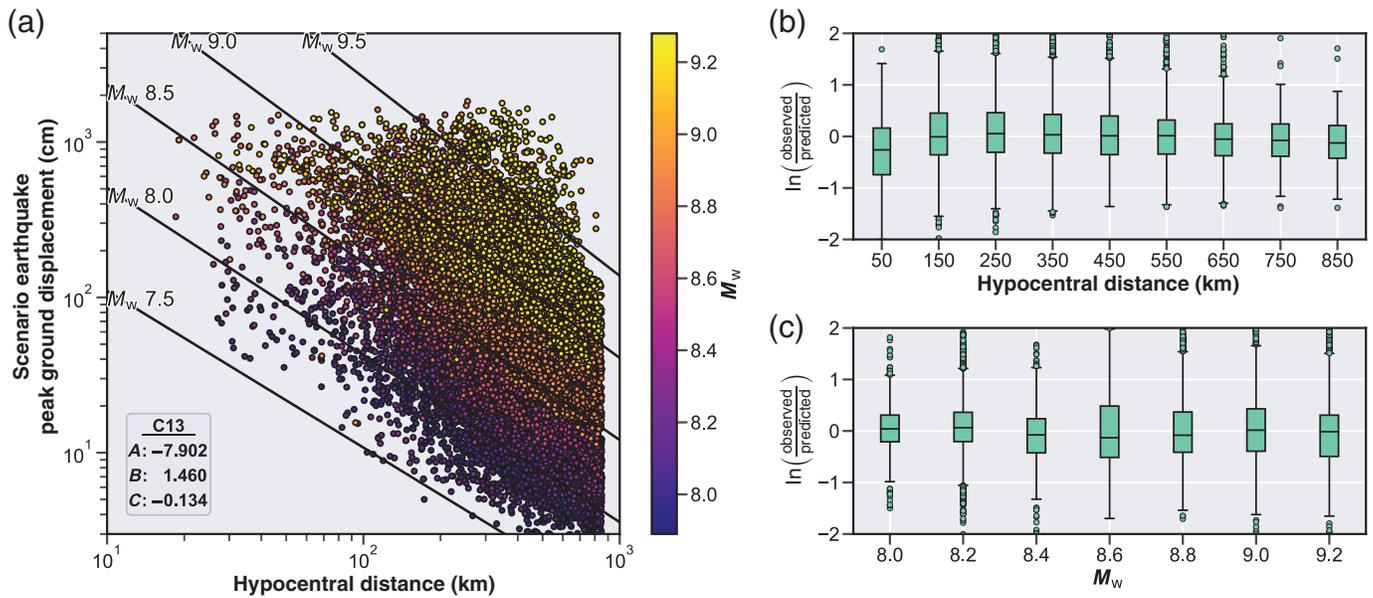


Figure 5. GMM C13 for Cascadia scenario events using hypocentral distance metric: (a) synthetic GNSS waveform PGD versus the hypocentral distance at which that station was located and colored by the magnitude of the associated scenario earthquake. PGD values shown have been adjusted by their corresponding site and event terms. Black lines represent the best-fitting scaling relation (C13) for these synthetic data; (b) residual (equation 7) as a function of hypocentral distance; and (c) residual as a function of scenario earthquake magnitude.

distance metric $R_p^{-4.5}$ are available in Table 3. Conversely, the Cascadia scenario data set is best fit by model C13 with the distance metric $R_p^{-2.3}$ (Figs. 6a and 7). Notably, although the difference in residuals for the observed earthquake data set is minimal across both the considered range of powers of the mean and the use of R_{hyp} , the IQR of Cascadia scenario event residuals is much lower when R_p is used in place of R_{hyp} . Although there is little variation in the residuals across the values of the power of the mean considered, this data set clearly favors a power of the mean lower than -1.5 , with -2.3 as the value of power of the mean that minimizes the residuals. The resulting equation coefficients and standard deviations (equation 5) for each of these cases is available in Table 4.

Finally, we apply the GMM formulation of TB18 to the Cascadia scenario events. The fits to the synthetic data are especially poor using the distance metric R_{hyp} (Figs. 6a and 8) and once again improved using the distance metric R_p . In this case, the power of the mean that minimizes the residual IQR is -1.7 : $R_p^{-1.7}$ (Fig. 9). The resulting coefficients and standard deviations (equation 5) for both of these cases are listed in Table 5. Overall, the TB18 formulation fits the synthetic scenario data set worse than the more simplistic C13 formulation (Fig. 6).

DISCUSSION

The consistency with which the observed earthquake data set is fit regardless of distance metric used in functional form C13 (R_{hyp} or values of R_p) speaks to the substantial limitations of that data set to define a robust GMM. Despite the growing availability of HR-GNSS observations of moderate- to large-magnitude earthquakes, it remains true that 90% of the observations for $M_w > 8$ earthquakes come from only two events: 2011 M_w 9.1 Tohoku-Oki and 2003 M_w 8.3 Tokachi-Oki, both shallow thrust events in Japan where the Pacific plate subducts

beneath the overriding Okhotsk microplate. Furthermore, though PGD is visible above the GNSS noise out to at least 678 km hypocentral distance for the M_w 9.1 Tohoku-Oki earthquake and at least 549 km hypocentral distance for the M_w 8.3 Tokachi-Oki earthquake, there is a dearth of truly near-field (within one fault length) observations. The M_w 8.3 Tokachi-Oki earthquake has an equivalent fault length (Mai and Beroza, 2000) of 141 km and only four observations within that distance (closest station at a hypocentral distance of 110 km). The Tohoku-Oki event has an equivalent fault length of 318 km, and whereas there exist 178 observations within one fault length (closest station at 81 km and 62 stations within 200 km) that still represents only one-third (34%) of the observations for that event. These two events have another important characteristic in common; they are both bilateral ruptures, with the maximum slip occurring at a similar location along strike as the hypocenter. This suggests that R_{hyp} is a sufficiently good predictor of dynamic motions for bilateral ruptures, as long as observations are not too close to the rupture itself.

Because of the global distribution of earthquakes and the limited time range of observations, relatively few stations observed multiple earthquakes (Fig. 3). The mixed-effects approach compensates by reducing the station bias (site terms) and increasing the station uncertainty. As such, the estimated

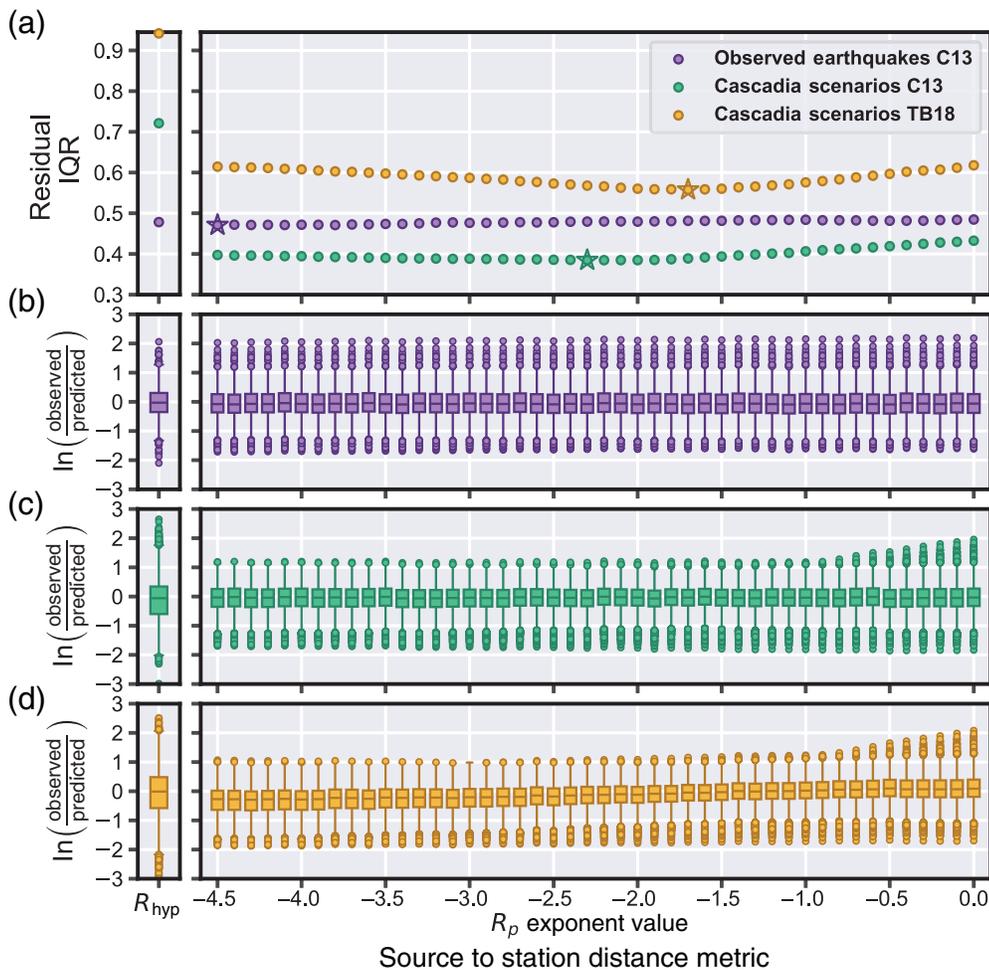


Figure 6. Comparison between distance metrics (left: hypocentral distance, R_{hyp} ; right: generalized mean rupture distance, R_p) using the C13 formulation (Crowell *et al.*, 2013) for the observed earthquake data set (purple) and the Cascadia scenario data set (green) in addition to the TB18 formulation (Thompson and Baltay, 2018) for the Cascadia scenario data set (orange). (a) Interquartile range (IQR) measurement of residual (equation 7) between the observed PGD and the PGD predicted from the best-fitting set of coefficients. Stars denote the distance metric that returns the lowest residual IQR. Colors are consistent in the remaining subplots: (b) full residual results for the observed earthquakes and the C13 formulation (purple), (c) full residual results for Cascadia scenario events and the C13 formulation (green), and (d) full residual results for the Cascadia scenario events and the TB18 formulation (orange).

site terms are small (order 10^{-5}), with uncertainties roughly 2 orders of magnitude larger than the estimates themselves. Event terms are available in Table 3. As an example, the positive event term for the 2011 M_w 9.1 Tohoku-Oki earthquake suggests that the event has larger PGD values than a “typical” magnitude 9 event. This in conjunction with previous suggestions that P -wave amplitude grows uncharacteristically slowly for this event (Trugman *et al.*, 2019; Goldberg and Melgar, 2020) contributes to our understanding that the Tohoku-Oki event grew slowly at first, but eventually grew to become a large-displacement M_w 9 event.

The importance of rupture directivity (bilateral vs. unilateral) becomes increasingly clear when we consider the Cascadia scenario events. In these scenarios, the hypocenter

location is selected at random from within the region that slips, resulting in a variety of bilateral and unilateral ruptures. Notably, this random assignment of the hypocenter location results in a greater proportion of unilateral ruptures than what is seen in the large-magnitude earthquake catalog (Melgar and Hayes, 2019). PGD ground-motion scaling that uses hypocentral distance performs especially poorly on unilateral ruptures (Williamson *et al.*, 2020; Fig. 5). However, the preference of large-magnitude earthquakes to manifest as bilateral ruptures in our existing catalog should not discourage us from adjusting our GMM to accommodate unilateral ruptures, as is clearly accomplished with a simple switch to the generalized mean rupture distance (Fig. 7). Though seemingly rare, large unilateral events have happened and must be anticipated in the future. The 2004 M_w 9.2 Sumatra earthquake is the most notable example in recent history, with a clear northward migration of rupture over the ~ 8 -minute-long event (Ishii *et al.*, 2005) (the 2004 M_w 9.2 Sumatra earthquake was not observed with HR-GNSS and is, therefore, not included in our data

set). Although a more complex distance metric such as R_p is not required by the observed earthquake data set, this data set is nearly equally well fit by all distance metrics considered. Thus, it is sensible to adopt the distance metric $R_p^{-2.3}$ for future ground-motion modeling, as it is more physical and better able to accommodate a larger suite of rupture styles, including those not represented in the existing observed earthquake data set. This value is also consistent with the finding by Thompson and Baltay (2018) that longer period intensity measures prefer lower values of the power of the mean, p (see fig. 5 of that paper). Although it is not straightforward to assign an equivalent period to the observation of PGD, a good estimate is likely > 10 s, for which Thompson and Baltay (2018) found that $p \approx -2.4$ fit best.

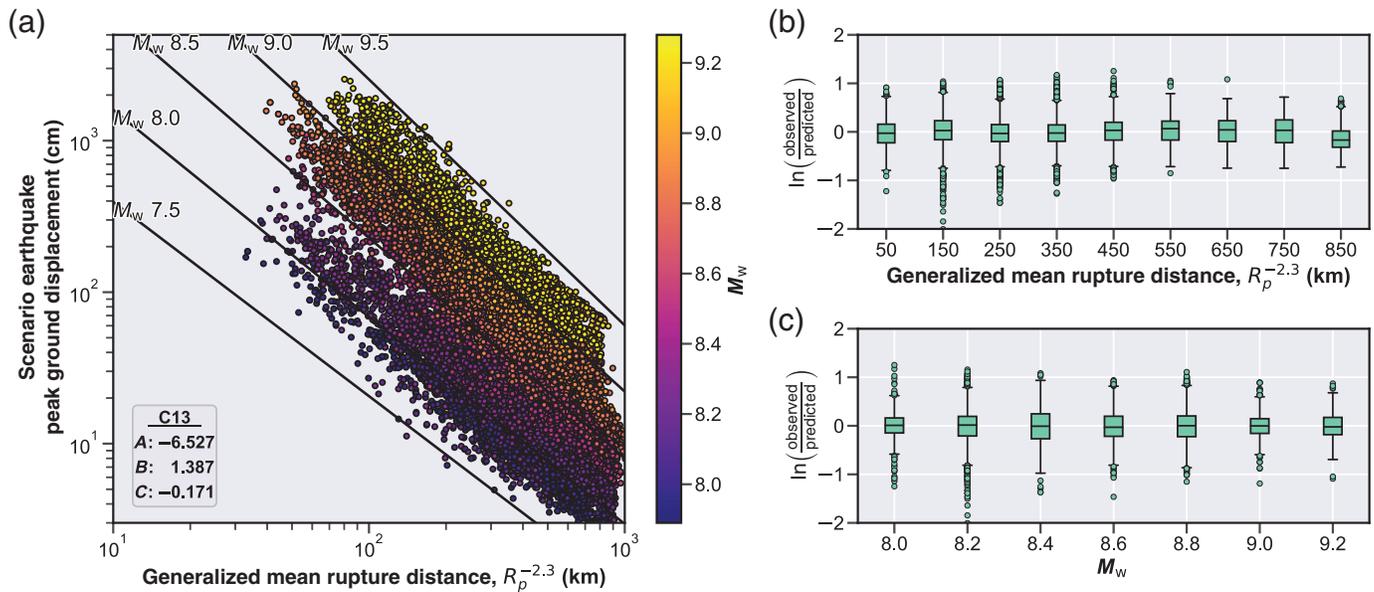


Figure 7. GMM C13 for Cascadia scenario events using generalized mean rupture distance with power of the mean equal to -2.3 ($R_p^{-2.3}$): (a) synthetic GNSS waveform PGD versus generalized mean rupture distance, $R_p^{-2.3}$, at which the station was located and colored by the magnitude of the associated scenario earthquake. PGD values shown have been adjusted by

their corresponding site and event terms. Black lines represent the best-fitting scaling relation (C13) for these synthetic data; (b) residual (equation 7) as a function of generalized mean rupture distance, $R_p^{-2.3}$; and (c) residual as a function of scenario earthquake magnitude.

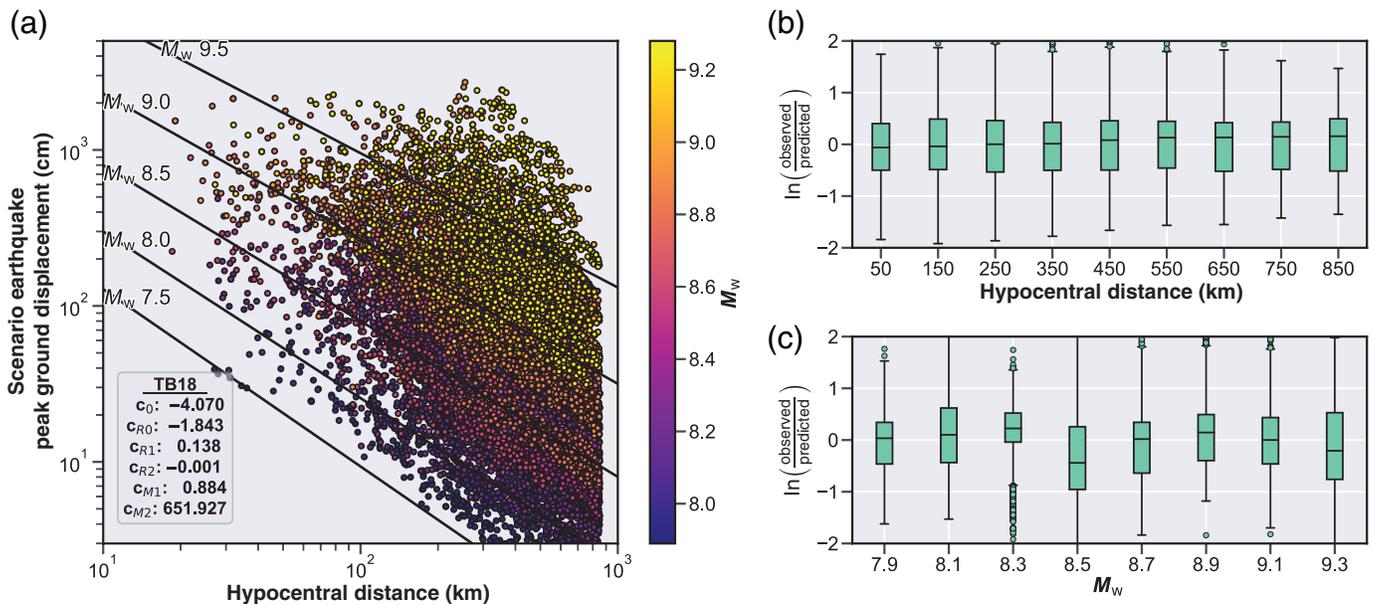
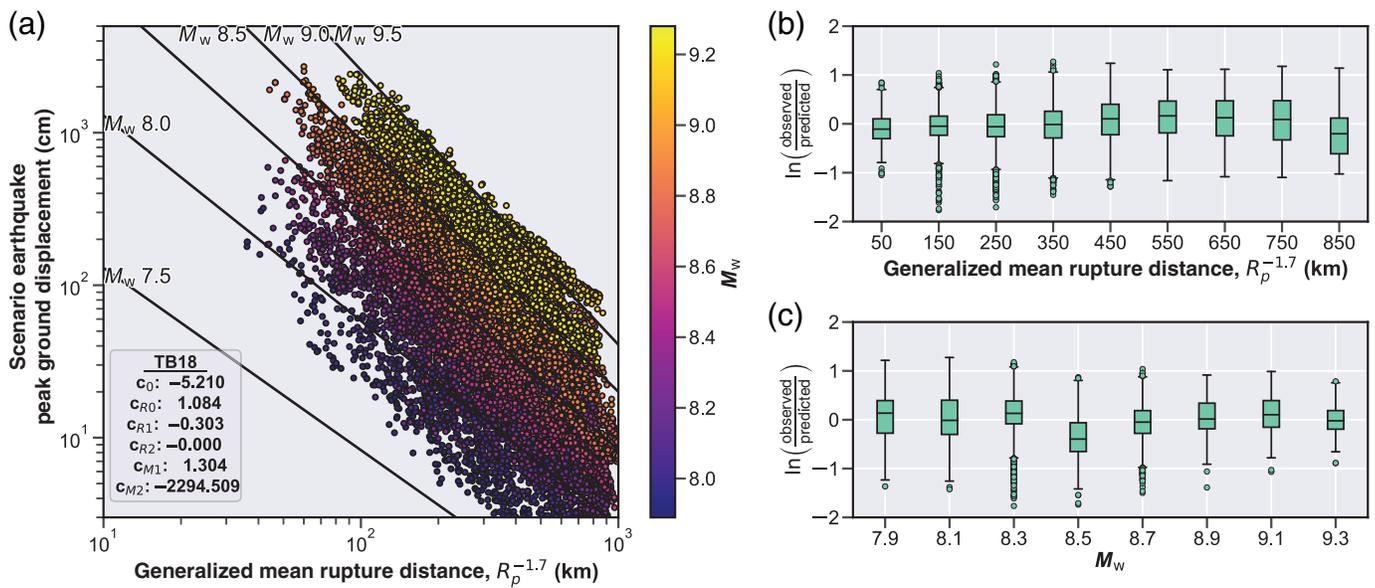


Figure 8. GMM TB18 for Cascadia scenario events, using hypocentral distance metric: (a) synthetic GNSS waveform PGD versus the hypocentral distance at which that station was located and colored by the magnitude of the associated scenario earthquake. PGD values shown have been adjusted

by their corresponding site and event terms. Black lines represent the best-fitting scaling relation (TB18) for these synthetic data; (b) residual (equation 7) as a function of hypocentral distance; and (c) residual as a function of scenario earthquake magnitude.

Within the synthetic Cascadia scenario data set, event terms likely represent source features, unique to the heterogeneity of the *FakeQuakes* parameters. Because each scenario event is recorded by nearly all sites, these terms are very well constrained

and have small uncertainties. Site terms in this data set are unique from the observed data set in that the stations each record significantly more earthquakes; however, all synthetic waveforms are created using a 1D velocity model. As such, it is



unclear how well these represent realistic PGD site terms as there should not be any persistent local effects. In addition, PGD site terms are not well understood; because PGD is a lower-frequency ground-motion feature, shallow site characteristics likely do not affect the resulting site terms. It is important to note that the uncertainties we find in all PGD models here (observed or synthetic data) are lower than those reported from both small- and large-magnitude GMMs for SM or velocity intensity measures (Tables 4 and 5; Sahakian *et al.*, 2018; Kotha *et al.*, 2020; Weatherill *et al.*, 2020). We observe uncertainties nearly half that of these other models. This could possibly be due to the smaller nature of our data set in comparison to these other models, but more likely is due to the nature of the intensity measures themselves. PGD is a much lower-frequency metric than PGA, PGV, or SAs, and therefore is likely less susceptible to small-scale source, path, and site characteristics that cause unmodeled randomness or variability (Sahakian, Melgar, and Muzli, 2019).

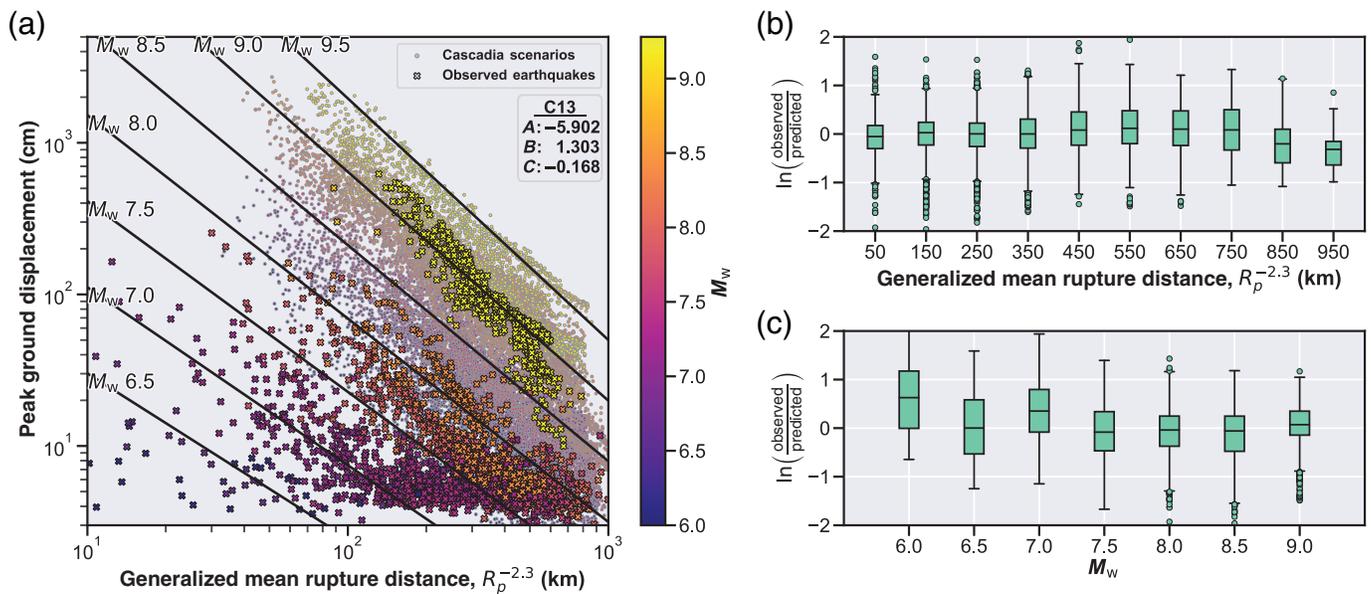
It is especially interesting that GMM form C13 performs better than form TB18 in describing the Cascadia scenario events, despite the additional parameters available. The TB18 model performs especially poorly using the hypocentral distance metric (which we note was never the intention of this GMM proposed by Thompson and Baltay, 2018). One expects a

Figure 9. GMM TB18 for Cascadia scenario events, using generalized mean rupture distance with power of the mean equal to -1.7 ($R_p^{-1.7}$): (a) synthetic GNSS waveform PGD versus generalized mean rupture distance, $R_p^{-1.7}$, at which the station was located and colored by the magnitude of the associated scenario earthquake. PGD values shown have been adjusted by their corresponding site and event terms. Black lines represent the best-fitting scaling relation (TB18) for these synthetic data; (b) residual (equation 7) as a function of generalized mean rupture distance, $R_p^{-1.7}$; and (c) residual as a function of scenario earthquake magnitude.

PGD GMM to clarify that at large distance from any magnitude earthquake, PGD will tend to zero or the instrument noise floor (imagine the black lines eventually merging past the bottom right corner of Fig. 7a). However, the best-fitting model in this case instead predicts that all magnitude earthquakes will experience the same (high-amplitude) PGD at some very close distance to the fault (imagine the black lines merging to the left of Fig. 8a). Similarly, the model shows a persistent bias in distance, with the median residual consistently >0 at hypocentral distances beyond 350 km (Fig. 8b). The reason is that the model is attempting to fit the saturation in ground-motion amplitudes observed at near-fault distances, where displacements approach the amplitude of slip on the fault itself, as well as the distance attenuation. This quality has led previous GMMs to include an

TABLE 5
GMM Coefficients and Standard Deviations for Functional Form TB18 for Distance Metrics of Interest: R_{hyp} and R_p with Power of the Mean that Minimizes Residual IQR, $R_p^{-1.7}$

Data Set	Distance Metric	c_0	c_{R0}	c_{R1}	c_{R2}	c_{M1}	c_{M2}	σ	τ	ϕ_S	ϕ_{SS}
Cascadia scenario earthquakes	R_{hyp}	-4.070	-1.843	0.138	-6×10^{-4}	0.884	652	0.299	0.163	0.033	0.248
	$R_p^{-1.7}$	-5.210	1.084	-0.303	-1×10^{-5}	1.304	-2295	0.194	0.132	0.033	0.138



additional near-source saturation term to measure observation distance as the hypotenuse of the minimum distance metric and a *saturation term* (e.g., the “fictitious depth,” defined by [Boore et al., 1997](#)). Using R_p eliminates the need for such a term, as was first shown by [Thompson and Baltay \(2018\)](#) and confirmed here (Fig. 9). The use of the generalized mean rupture distance not only allows functional form TB18 to fit the data set in a way that confirms that PGD will tend to zero at a sufficient distance from any size earthquake, but it also reduces the consistency of the distance-related bias (Fig. 9b) discussed earlier.

Because of the poorer fits that form TB18 offers in comparison to form C13 (Fig. 6a), form C13 is preferable for both model performance and reducing model complexity. Slight differences between the best-fitting coefficients for the observed earthquake and scenario data sets may be due to the lack of variation in earthquake mechanism in the scenario events, all of which are thrust earthquakes. Although thrust events account for the vast majority of great magnitude earthquakes ($M_w > 8$), future work is needed to clarify whether including a variety of scenario earthquake mechanisms (strike slip, normal, and oblique) and locations (for different seismic-velocity profiles as well as different azimuthal station coverage) may indicate a different set of preferred GMM coefficients. In the meantime, we calculate one final set of coefficients for the C13 GMM using the currently available observed and scenario data sets simultaneously (Fig. 10). We recommend these coefficients (see Table 4) for GMM implementation of future earthquakes and for testing of synthetic data sets. We note some bias in the joint solution, but find it appropriate for distances <750 km, which is sufficient for the purpose of regional ground-motion modeling, and magnitudes ≥ 7.5 , where GNSS is most needed to complement seismic observations at regional distances.

Figure 10. GMM C13 for both observed earthquake data set and Cascadia scenario events, using generalized mean rupture distance with power of the mean equal to -2.3 ($R_p^{-2.3}$): (a) waveform PGD versus generalized mean rupture distance, $R_p^{-2.3}$, at which the station was located. Synthetic observations of the Cascadia scenario events are shown as small circles, overlain by the observed earthquake data set, shown as cross marks. Both are colored by the magnitude of the associated observed or scenario earthquake. PGD values shown have been adjusted by their corresponding site and event terms. Black lines represent the best-fitting scaling relation (C13) for these data; (b) residual (equation 7) as a function of generalized mean rupture distance, $R_p^{-2.3}$; and (c) residual as a function of earthquake magnitude.

CONCLUSIONS

We have presented an updated GMM based on PGD observations from HR GNSS at regional distances from earthquakes M_w 6–9. We find that the available observed earthquake data set is nearly equally well fit by GMMs that rely on hypocentral distance and those that rely on generalized mean rupture distance, including over a range of powers of the mean. By including scenario ruptures and associated synthetic displacement waveforms to supplement the available observed earthquake data set, we find that, in particular, very near-source observations and especially observations of unilateral ruptures have strong preference for a model that utilizes the generalized mean rupture distance instead of a simplistic hypocentral distance metric. However, the more complex TB18 GMM with six parameters, tested against the scenario events, does not improve upon the originally developed C13 magnitude-scaling law (three parameters). We find that the best and simplest model is based on the [Crowell et al. \(2013\)](#) model, simply substituting generalized mean rupture distance with power of the mean equal to -2.3 . This creates an earthquake GMM that fits not only the events

in our observed earthquake data set, but also the scenario events that rupture in unique ways not yet observed with GNSS data.

DATA AND RESOURCES

The Cascadia scenario ruptures and synthetic Global Navigation Satellite Systems (GNSS) waveforms are publicly available at <https://zenodo.org/record/59943> (last accessed January 2021; Melgar *et al.*, 2016). The observed earthquake GNSS data in miniSEED format, text files with station location information, and peak ground displacement (PGD) values, as well as the slip models considered for each event are preserved at <https://www.sciencebase.gov/catalog/item/60ca3d3bd34e86b938a10659> (last accessed July 2021; see Goldberg *et al.*, 2021).

DECLARATION OF COMPETING INTERESTS

The authors acknowledge there are no conflicts of interest recorded.

ACKNOWLEDGMENTS

The authors thank Amy Williamson for her help with the Cascadia scenario data set. They also thank the Guest Editors for the Special Section on Fault Displacement and Near-Source Ground-Motion Models, Gail Atkinson, Luis A. Dalguer, Steven Day, and Rui Chen, as well as reviewers R. Martin Mai, Eric Thompson, and Annemarie Baltay for their helpful reviews of this work, which have improved the quality of this article.

REFERENCES

- Al Atik, L., J. Bommer, F. Scherbaum, F. Cotton, and N. Kuehn (2010). The variability of ground-motion prediction models and its components, *Seismol. Res. Lett.* **81**, no. 5, 795–801, doi: [10.1785/gssrl.81.5.794](https://doi.org/10.1785/gssrl.81.5.794).
- Allen, T. I., and G. P. Hayes (2017). Alternative rupture-scaling relationships for subduction interface and other offshore environments, *Bull. Seismol. Soc. Am.* **107**, no. 3, 1240–1253, doi: [10.1785/0120160255](https://doi.org/10.1785/0120160255).
- Barbour, A. J., and B.W. Crowell (2017). Dynamic strains for earthquake source characterization, *Seismol. Res. Lett.* **88**, no. 2A, 354–370, doi: [10.1785/0220160155](https://doi.org/10.1785/0220160155).
- Bertiger, W., Y. Bar-Sever, A. Dorsey, B. Haines, N. Harvey, D. Hemberger, M. Heflin, W. Lu, M. Miller, A. W. Moore, *et al.* (2020). GipsyX/RTGx, a new tool set for space geodetic operations and research, *Adv. Space Res.* **66**, no. 3, 469–489, doi: [10.1016/j.asr.2020.04.015](https://doi.org/10.1016/j.asr.2020.04.015).
- Blaser, L., F. Krüger, M. Ohrnberger, and F. Scherbaum (2010). Scaling relations of earthquake source parameter estimates with special focus on subduction environment, *Bull. Seismol. Soc. Am.* **100**, no. 6, 2914–2926, doi: [10.1785/0120100111](https://doi.org/10.1785/0120100111).
- Boore, D. M., and J. J. Bommer (2005). Processing of strong-motion accelerograms: Needs, options and consequences, *Soil Dynam. Earthq. Eng.* **25**, no. 2, 93–115, doi: [10.1016/j.soildyn.2004.10.007](https://doi.org/10.1016/j.soildyn.2004.10.007).
- Boore, D. M., W. B. Joyner, and T. E. Fumal (1997). Equations for estimating horizontal response spectra and peak acceleration from western North American earthquakes: A summary of recent work, *Seismol. Res. Lett.* **68**, no. 1, 128–153, doi: [10.1785/gssrl.68.1.128](https://doi.org/10.1785/gssrl.68.1.128).
- Campbell, K. W., and Y. Bozorgnia (2008). NGA ground motion model for the geometric mean horizontal component of PGA, PGV, PGD and 5% damped linear elastic response spectra for periods ranging from 0.01 to 10 s, *Earthq. Spectra* **24**, no. 1, 139–171, doi: [10.1193/1.2857546](https://doi.org/10.1193/1.2857546).
- Chousianitis, K., A. O. Konca, G.-A. Tselentis, G. A. Papadopoulos, and M. Gianniu (2016). Slip model of the 17 November 2015 $M_w = 6.5$ Lefkada earthquake from the joint inversion of geodetic and seismic data, *Geophys. Res. Lett.* **43**, no. 15, 7973–7981, doi: [10.1002/2016GL069764](https://doi.org/10.1002/2016GL069764).
- Crowell, B. W., Y. Bock, and D. Melgar (2012). Real-time inversion of GPS data for finite fault modeling and rapid hazard assessment, *Geophys. Res. Lett.* **39**, no. 9, doi: [10.1029/2012GL051318](https://doi.org/10.1029/2012GL051318).
- Crowell, B. W., D. Melgar, Y. Bock, J. S. Haase, and J. Geng (2013). Earthquake magnitude scaling using seismogeodetic data, *Geophys. Res. Lett.* **40**, no. 23, 6089–6094, doi: [10.1002/2013GL058391](https://doi.org/10.1002/2013GL058391).
- Crowell, B. W., D. A. Schmidt, P. Bodin, J. E. Vidale, J. Gomberg, J. Renate Hartog, V. C. Kress, T. I. Melbourne, M. Santillan, S. E. Minson, *et al.* (2016). Demonstration of the Cascadia G-FAST geodetic earthquake early warning system for the Nisqually, Washington, earthquake, *Seismol. Res. Lett.* **87**, no. 4, 930–943, doi: [10.1785/0220150255](https://doi.org/10.1785/0220150255).
- Goldberg, D. E., and Y. Bock (2017). Self-contained local broadband seismogeodetic early warning system: Detection and location, *J. Geophys. Res.* **122**, no. 4, 3197–3220, doi: [10.1002/2016JB013766](https://doi.org/10.1002/2016JB013766).
- Goldberg, D. E., and D. Melgar (2020). Generation and validation of broadband synthetic *P* waves in semistochastic models of large earthquakes, *Bull. Seismol. Soc. Am.* **110**, no. 4, 1982–1995, doi: [10.1785/0120200049](https://doi.org/10.1785/0120200049).
- Goldberg, D. E., D. Melgar, Y. Bock, and R. M. Allen (2018). Geodetic observations of weak determinism in rupture evolution of large earthquakes, *J. Geophys. Res.* **123**, no. 11, 9950–9962, doi: [10.1029/2018JB015962](https://doi.org/10.1029/2018JB015962).
- Goldberg, D. E., D. Melgar, and B. W. Crowell (2021). High-rate GNSS observations and finite fault models of moderate to large earthquakes, *U.S. Geol. Surv. Data Release*, doi: [10.5066/P905JY97](https://doi.org/10.5066/P905JY97).
- Goldberg, D. E., D. Melgar, V. J. Sahakian, A. M. Thomas, X. Xu, B. W. Crowell, and J. Geng (2020). Complex rupture of an immature fault zone: A simultaneous kinematic model of the 2019 Ridgecrest, CA earthquakes, *Geophys. Res. Lett.* **47**, no. 3, e2019GL086382, doi: [10.1029/2019GL086382](https://doi.org/10.1029/2019GL086382).
- Grapenthin, R., M. West, and J. Freymueller (2017). The utility of GNSS for earthquake early warning in regions with sparse seismic networks, *Bull. Seismol. Soc. Am.* **107**, no. 4, 1883–1890, doi: [10.1785/0120160317](https://doi.org/10.1785/0120160317).
- Hayes, G. P. (2017). The finite, kinematic rupture properties of great-sized earthquakes since 1990, *Earth Planet. Sci. Lett.* **468**, 94–100, doi: [10.1016/j.epsl.2017.04.003](https://doi.org/10.1016/j.epsl.2017.04.003).
- Hodgkinson, K. M., D. J. Mencin, K. Feaux, C. Sievers, and G. S. Mattioli (2020). Evaluation of earthquake magnitude estimation and event detection thresholds for real-time GNSS networks: Examples from recent events captured by the Network of the Americas, *Seismol. Res. Lett.* **91**, no. 3, 1628–1645, doi: [10.1785/0220190269](https://doi.org/10.1785/0220190269).
- Ishii, M., P. M. Shearer, H. Houston, and J. E. Vidale (2005). Extent, duration and speed of the 2004 Sumatra–Andaman earthquake

- imaged by the Hi-Net array, *Nature* **435**, no. 7044, 933–936, doi: [10.1038/nature03675](https://doi.org/10.1038/nature03675).
- Konca, A. O., S. Cetin, H. Karabulut, R. Reilinger, U. Dogan, S. Ergintav, Z. Cakir, and E. Tari (2018). The 2014, M_w 6.9 North Aegean earthquake: Seismic and geodetic evidence for coseismic slip on persistent asperities, *Geophys. J. Int.* **213**, no. 2, 1113–1120, doi: [10.1093/gji/ggy049](https://doi.org/10.1093/gji/ggy049).
- Kotha, S. R., G. Weatherill, D. Bindi, and F. Cotton (2020). A regionally-adaptable ground-motion model for shallow crustal earthquakes in Europe, *Bull. Earthq. Eng.* **18**, no. 9, 4091–4125, doi: [10.1007/s10518-020-00869-1](https://doi.org/10.1007/s10518-020-00869-1).
- Mai, P. M., and G. C. Beroza (2000). Source scaling properties from finite-fault-rupture models, *Bull. Seismol. Soc. Am.* **90**, no. 3, 604–615, doi: [10.1785/0119990126](https://doi.org/10.1785/0119990126).
- Mai, P. M., and K. K. S. Thingbaijam (2014). SRCMOD: An online database of finite-fault rupture models, *Seismol. Res. Lett.* **85**, no. 6, 1348–1357, doi: [10.1785/0220140077](https://doi.org/10.1785/0220140077).
- Melgar, D., and G. P. Hayes (2019). The correlation lengths and hypocentral positions of great earthquakes, *Bull. Seismol. Soc. Am.* **109**, no. 6, 2582–2593, doi: [10.1785/0120190164](https://doi.org/10.1785/0120190164).
- Melgar, D., Y. Bock, D. Sanchez, and B. W. Crowell (2013). On robust and reliable automated baseline corrections for strong motion seismology, *J. Geophys. Res.* **118**, no. 3, 1177–1187, doi: [10.1002/jgrb.50135](https://doi.org/10.1002/jgrb.50135).
- Melgar, D., B. W. Crowell, J. Geng, R. M. Allen, Y. Bock, S. Riquelme, E. M. Hill, M. Protti, and A. Ganas (2015). Earthquake magnitude calculation without saturation from the scaling of peak ground displacement, *Geophys. Res. Lett.* **42**, no. 13, 5197–5205, doi: [10.1002/2015GL064278](https://doi.org/10.1002/2015GL064278).
- Melgar, D., B. W. Crowell, T. I. Melbourne, W. Szeliga, M. Santillan, and C. Scrivner (2020). Noise characteristics of operational real-time high-rate GNSS positions in a large aperture network, *J. Geophys. Res.* **125**, no. 7, e2019JB019197, doi: [10.1029/2019JB019197](https://doi.org/10.1029/2019JB019197).
- Melgar, D., J. Geng, B. W. Crowell, J. S. Haase, Y. Bock, W. C. Hammond, and R. M. Allen (2015). Seismogeodesy of the 2014 M_w 6.1 Napa earthquake, California: Rapid response and modeling of fast rupture on a dipping strike-slip fault, *J. Geophys. Res.* **120**, no. 7, 5013–5033, doi: [10.1002/2015JB011921](https://doi.org/10.1002/2015JB011921).
- Melgar, D., R. J. LeVeque, D. S. Dreger, and R. M. Allen (2016). Kinematic rupture scenarios and synthetic displacement data: An example application to the Cascadia subduction zone, *J. Geophys. Res.* **121**, no. 9, 6658–6674, doi: [10.1002/2016JB013314](https://doi.org/10.1002/2016JB013314).
- Melgar, D., A. Ruiz-Angulo, E. S. Garcia, M. Manea, V. C. Manea, X. Xu, M. T. Ramirez Herrera, J. Zavala-Hidalgo, J. Geng, N. Corona, et al. (2018). Deep embrittlement and complete rupture of the lithosphere during the M_w 8.2 Tehuantepec earthquake, *Nature Geosci.* **11**, no. 12, 955–960, doi: [10.1038/s41561-018-0229-y](https://doi.org/10.1038/s41561-018-0229-y).
- Petersen, M. D., T. E. Dawson, R. Chen, T. Cao, C. J. Wills, D. P. Schwartz, and A. Frankel (2011). Fault displacement hazard for strike-slip faults, *Bull. Seismol. Soc. Am.* **101**, no. 2, 805–825, doi: [10.1785/0120100035](https://doi.org/10.1785/0120100035).
- Ruhl, C. J., D. Melgar, J. Geng, D. E. Goldberg, B. W. Crowell, R. M. Allen, Y. Bock, S. Barrientos, S. Riquelme, J. C. Baez, et al. (2018). A global database of strong-motion displacement GNSS recordings and an example application to PGD scaling, *Seismol. Res. Lett.* **90**, no. 1, 271–279, doi: [10.1785/0220180177](https://doi.org/10.1785/0220180177).
- Sahakian, V., A. Baltay, T. Hanks, J. Buehler, F. Vernon, D. Kilb, and N. Abrahamson (2018). Decomposing leftovers: Event, path, and site residuals for a small-magnitude Anza region GMPE, *Bull. Seismol. Soc. Am.* **108**, no. 5A, 2478–2492, doi: [10.1785/0120170376](https://doi.org/10.1785/0120170376).
- Sahakian, V. J., A. Baltay, T. C. Hanks, J. Buehler, F. L. Vernon, D. Kilb, and N. A. Abrahamson (2019). Ground motion residuals, path effects, and crustal properties: A pilot study in Southern California, *J. Geophys. Res.* **124**, no. 6, 5738–5753.
- Sahakian, V. J., D. Melgar, and M. Muzli (2019). Weak near-field behavior of a tsunami earthquake: Toward real-time identification for local warning, *Geophys. Res. Lett.* **46**, no. 16, 9519–9528, doi: [10.1029/2019GL083989](https://doi.org/10.1029/2019GL083989).
- Tanaka, M., K. Asano, T. Iwata, and H. Kubo (2014). Source rupture process of the 2011 Fukushima-ken Hamadori earthquake: How did the two subparallel faults rupture? *Earth Planets Space* **66**, no. 1, Article Number 101, doi: [10.1186/1880-5981-66-101](https://doi.org/10.1186/1880-5981-66-101).
- Thingbaijam, K. K., P. M. Mai, and G. Katsuchihiro (2017). New empirical earthquake source-scaling laws, *Bull. Seismol. Soc. Am.* **107**, no. 5, 2225–2246, doi: [10.1785/0120170017](https://doi.org/10.1785/0120170017).
- Thompson, E. M., and A. S. Baltay (2018). The case for mean rupture distance in ground-motion estimation, *Bull. Seismol. Soc. Am.* **108**, no. 5A, 2462–2477, doi: [10.1785/0120170306](https://doi.org/10.1785/0120170306).
- Trugman, D. T., M. T. Page, S. E. Minson, and E. S. Cochran (2019). Peak ground displacement saturates exactly when expected: Implications for earthquake early warning, *J. Geophys. Res.* **124**, no. 5, 4642–4653, doi: [10.1029/2018JB017093](https://doi.org/10.1029/2018JB017093).
- Wald, D. J., B. C. Worden, V. Quitoriano, and K. L. Pankow (2005). ShakeMap manual: Technical manual, user’s guide, and software guide (version 1.0), *U.S. Geol. Surv. Techniques and Methods 12-A1*, 134 pp., doi: [10.3133/tm12A1](https://doi.org/10.3133/tm12A1).
- Weatherill, G., S. R. Kotha, and F. Cotton (2020). A regionally-adaptable “scaled backbone” ground motion logic tree for shallow seismicity in Europe: Application to the 2020 European seismic hazard model, *Bull. Earthq. Eng.* **18**, no. 11, 5087–5117, doi: [10.1007/s10518-020-00899-9](https://doi.org/10.1007/s10518-020-00899-9).
- Williamson, A. L., D. Melgar, B. W. Crowell, D. Arcas, T. I. Melbourne, Y. Wei, and K. Kwong (2020). Toward near-field tsunami forecasting along the Cascadia subduction zone using rapid GNSS source models, *J. Geophys. Res.* **125**, no. 8, e2020JB019636, doi: [10.1029/2020JB019636](https://doi.org/10.1029/2020JB019636).
- Zhang, H., D. Melgar, and D. E. Goldberg (2020). Magnitude calculation without saturation from strong-motion waveforms, *Bull. Seismol. Soc. Am.* **111**, no. 1, 50–60, doi: [10.1785/0120200133](https://doi.org/10.1785/0120200133).
- Zheng, X., Y. Zhang, R. Wang, L. Zhao, W. Li, and Q. Huang (2020). Automatic inversions of strong-motion records for finite-fault models of significant earthquakes in and around Japan, *J. Geophys. Res.* **125**, no. 9, e2020JB019992, doi: [10.1029/2020JB019992](https://doi.org/10.1029/2020JB019992).

Manuscript received 21 February 2021

Published online 24 August 2021